ACS OMEGA

Open Access

http://pubs.acs.org/journal/acsodf

Article

An Efficient p−n Heterojunction Copper Tin Sulfide/g-C_3N_4 Nanocomposite for Methyl Orange Photodegradation

Endale Kebede Feyie, Enyew Amare Zereffa, Aschalew Tadesse, Mahendra Goddati, Daegwon Noh, Eunsoon Oh, Lemma Teshome Tufa,* and Jaebeom Lee*

Cite This: *ACS Omega* 2024, 9, 28463−28475

Read Online

ACCESS | Metrics & More | Article Recommendations | Supporting Information

ABSTRACT: The discharge of toxic dye effluents from industry is a major concern for environmental pollution and toxicity. These toxic dyes can be efficiently removed from waste streams using a photocatalysis process involving visible light. Due to its simple synthesis procedure, inexpensive precursor, and robust stability, graphitic carbon nitride (g-C_3N_4, or CN) has been used as a visible light responsive catalyst for the degradation of dyes with mediocre performance because it is limited by its low visible light harvesting capability due to its wide bandgap and fast carrier recombination rate. To overcome these limitations and enhance the performance of g-C_3N_4, it was coupled with a narrow bandgap copper tin sulfide (CTS) semiconductor to form a p−n heterojunction. CTS and g-C_3N_4 were selected due to their good stability, low toxicity, ease of synthesis, layered sheet/plate-like morphology, and relatively abundant precursors. Accordingly, a series of copper tin sulfide/graphitic carbon nitride nanocomposites (CTS/g-C_3N_4) with varying CTS contents were successfully synthesized via a simple two-step process involving thermal pyrolysis and coprecipitation for visible-light-induced photocatalytic degradation of methyl orange (MO) dye. The photocatalytic activity results showed that the 50%(wt/wt) CTS/g-C_3N_4 composite displayed a remarkable degradation efficiency of 95.6% for MO dye under visible light illumination for 120 min, which is higher than that of either pristine CTS or g-C_3N_4. The improved performance is attributed to the extended light absorption range (due to the optimized bandgap), effective suppression of photoinduced electron−hole recombination, and improved charge transfer that arose from the formation of a p−n heterojunction, as evidenced by electrochemical impedance spectroscopy (EIS), photocurrent, and photoluminescence results. Moreover, the results of the reusability study showed that the composite has excellent stability, indicating its potential for the degradation of MO and other toxic organic dyes from waste streams.

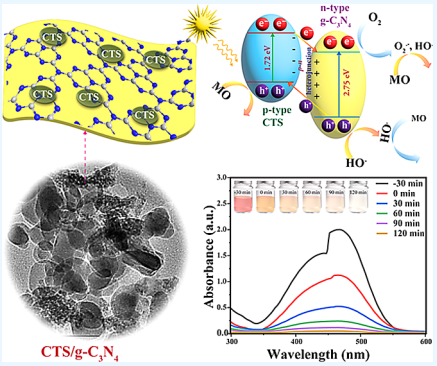

1. INTRODUCTION

Chromophoric dyes are usually used in the textile and paper industry due to their robust chemical stability.[1−3] Industrial wastewater containing dyes discharged into surface and groundwater environments affects the health of both humans and animals.[4,5] To mitigate the effects of these pollutants and comply with regulations, various physical,[6,7] biological,[3,8] chemical,[9,10] catalytic, and photocatalytic techniques have been developed for the removal and degradation of dyes in wastewater.

Photocatalysis, with ideal photoactive materials, has been attractive for the complete degradation of pollutant dyes.[7] Photocatalytic materials such as metal oxides (TiO_2[11,12] and ZnO[1,13]), metal sulfides (CdS[14] and $ZnIn_2S_4$[15]), and nonmetallic nitrides such as graphitic carbon nitride[16,17] have been employed. TiO_2 has been widely used in photocatalysis due to its remarkable catalytic performance, low cost, nontoxicity, and excellent stability under ultraviolet light illumination, which comprises 4% of the solar spectrum. However, it is not effective under solar light illumination due to its wide bandgap of 3.2 eV.[11,12] On the contrary, metal sulfides such as CdS and $ZnIn_2S_4$ are responsive to visible light and are considered the best due to their narrow bandgaps and acceptable light absorption coefficients in the visible range of the solar spectrum.[15] However, several factors, including photoinstability, photocorrosion, aggregation, and high charge recombination rates, limit their applicability as photocatalysts. In addition, the use of toxic and rare earth elements is unsatisfactory on environmental and economic scale-up.[18]

Accordingly, graphitic carbon nitride (g-C_3N_4, denoted as carbon nitride (CN)) is a promising metal-free 2D semiconductor material that has been used as a visible light photoresponsive catalyst for the degradation of dyes and can be considered an excellent alternative due to its simple synthesis procedure, low toxicity, and robust chemical and

Received: March 12, 2024
Revised: May 27, 2024
Accepted: May 31, 2024
Published: June 17, 2024

photostability.[16,17] Unfortunately, CN is not as efficient as other photocatalysts due to its poor absorption of visible light, wider bandgap (2.75 eV), higher carrier recombination rate, and low electrical conductivity.[19−24] This limitation can be overcome by forming a p-n heterojunction composite with a narrow bandgap semiconductor such as CTS. The coupling of p- and n-type semiconductors has been shown to enhance photocatalytic activity due to the buildup of an internal electric field across the junction which helps minimize the recombination of charge carriers by promoting the directional flow of photoinduced electrons and holes.[25−27] Recently, the synthesis of CTS (Cu_3SnS_4, Cu_2SnS_3), a p-type semiconductor, has been fascinating as an emerging material in the fields of photovoltaics[28,29] and photocatalysis[30−38] owing to its high visible light absorption coefficient (~10^4 cm^{-1}),[35,39] excellent electrical conductivity (with a hole density reaching up to ~10^{22} cm^{-3}),[36] narrow bandgap (<1.8 eV),[35,36] layered morphology, and reliable chemical and photostability.[32,33] In addition, CTS is composed of elements that are less toxic and more abundant in the Earth's crust, making it a viable candidate for economic and environmental scale-up. In recent years, several studies have demonstrated the photocatalytic activity of CTS compounds for the degradation of methyl orange (MO) dye with promising results, with Cu_3SnS_4 exhibiting the highest performance.[35,39−41]

Coupling of CTS with CN results in a narrowed bandgap-inducing improved light harvesting, in addition to reinforced charge separation and transport across the junction through the formation of a p−n heterojunction.[39] Hence, compared with either pristine CN or CTS, the CTS/CN composite exhibited an enhanced photocatalytic efficiency for the degradation of the MO dye. Currently, there are few works related to the synthesis and application of CTS/CN composites for the photocatalytic degradation of pollutants. For example, Tian et al. reported the application of a CN/CTS composite for the photocatalytic degradation of methyl blue dye with an 82.7% degradation efficiency achieved under visible light irradiation for 3.5 h, which is higher than that of either pristine CTS (52.4%) or CN (24.4%).[38] Olalekan and Olatunde also reported the use of CTS/CN composite for the degradation of tetracycline under ultraviolet (UV) light illumination, achieving a maximum degradation efficiency of 85.2%.[42] Both studies showed that the performance of the composite was enhanced relative to that of the pristine components, but such an efficiency was obtained at the expense of extended irradiation time. To the best of our knowledge, no work has been reported on the facile synthesis approach and application of CTS/CN composites for the photocatalytic degradation of the MO dye.

In this article, we report the synthesis of a CTS/CN composite nanomaterial as an efficient photocatalyst for the degradation of MO dye under visible light illumination. CN, CTS, and CTS/CN composites with various ratios of CTS (% wt/wt) ranging from 20 to 60% were synthesized to investigate their photocatalytic activity. Apart from the photocatalytic activity, the recyclability potential was also evaluated by subjecting the best performing composite to five consecutive photocatalytic cycles. It can be concluded from this study that the CTS/CN composite material is a remarkably efficient and stable visible light responsive photocatalyst for the degradation of the MO dye.

2. EXPERIMENTAL SECTION

2.1. Materials. Urea, tin(IV) chloride tetrahydrate ($SnCl_4·4H_2O$; 98%), copper(II) acetate monohydrate ($Cu(CH_3COO)_2·H_2O$; >98%), sodium sulfide nonahydrate ($Na_2S·9H_2O$; 98%), methyl orange dye (97%), hydrogen peroxide (H_2O_2, 30%(v/v)), ethanol (99%), dimethylformamide (DMF; 99.8%), fluorine-doped tin oxide (FTO) glass substrate (1 cm × 1.5 cm) potassium hexacyanoferrate (II) trihydrate ($K_4[Fe(CN)_6]·3H_2O$; 98.5%), potassium hexacyanoferrate (III) ($K_3[Fe(CN)_4]$; 99%), potassium chloride (KCl, 99%), and sodium sulfite (Na_2SO_3; 98%) were used for synthesis and characterization. Reactive species scavengers, isopropanol (IPA), EDTA tetrasodium salt, and *p*-benzoquinone (PBQ) were also used for reactive species identification. All reagents were of analytical grade, used without further purification, and acquired from JDH Chemicals, China. Deionized (DI) water was used throughout all of the experiments.

2.2. Synthesis of CN. CN was synthesized via the pyrolysis of urea with slight modifications to previously reported procedures.[43,44] Briefly, 20 g of urea was first placed in a porcelain crucible, covered with a lid, and then sealed by wrapping it with multiple layers of aluminum foil. The sealed precursor was then placed directly in a muffle furnace, heated to 550 °C at a rate of 15 °C/min, held at that temperature for 4 h, and finally allowed to cool to room temperature. The crucible was then unwrapped of the aluminum foil, and a fluffy pale-yellow powder was obtained.

2.3. Synthesis of CTS. CTS was synthesized via coprecipitation of Cu^{2+} and Sn^{4+} precursors using sodium sulfide as a precipitating agent following the procedure reported in refs 45 and 46. Briefly, 0.299 g of $Cu(CH_3COO)_2·H_2O$ and 0.176 g of $SnCl_4·4H_2O$ were added to a 250 mL beaker, containing 100 mL of distilled water, and stirred vigorously for 30 min using a magnetic stirrer. The solution was then heated to 80 °C, followed by the slow addition of a 0.1 M Na_2S solution from a buret while stirring continuously. The mixture was then allowed to cool and digest for 3 h. The solution was then centrifuged to separate the precipitate, and the precipitate was then washed three times successively with ethanol and deionized water, respectively. Finally, the precipitate was dried overnight in a vacuum oven at 60 °C.

2.4. Synthesis of CTS/CN Composites. The CTS/CN composite photocatalysts were prepared by the coprecipitation method. Briefly, for preparing 20%wt/wt CTS/CN composite, 0.70 g of CN and stoichiometric amounts of $SnCl_4·4H_2O$ and $Cu(CH_3CO_2)_2·H_2O$ were added to 250 mL beaker, dissolved in 100 mL of distilled water, and sonicated for 30 min to disperse the precursors uniformly. The mixture was then heated to 80 °C, followed by the slow addition of a 0.1 M Na_2S solution from a buret while stirring continuously. The mixture was allowed to cool and digest for 3 h. The solution was then centrifuged, and the isolated precipitate was subjected to the same washing procedure described above. Finally, the precipitate was dried overnight in a vacuum oven at 60 °C. A series of CTS/CN composites with varying contents of CTS (20−60%wt/wt) were prepared and labeled as CTS/CN, 20CTS/CN, 30CTS/CN, 40CTS/CN, 50CTS/CN, and 60CTS/CN.

2.5. Material Characterization. Powder X-ray diffraction (XRD) analysis was performed on a Shimadzu Maxima 7000

https://doi.org/10.1021/acsomega.4c02414
ACS Omega 2024, 9, 28463−28475

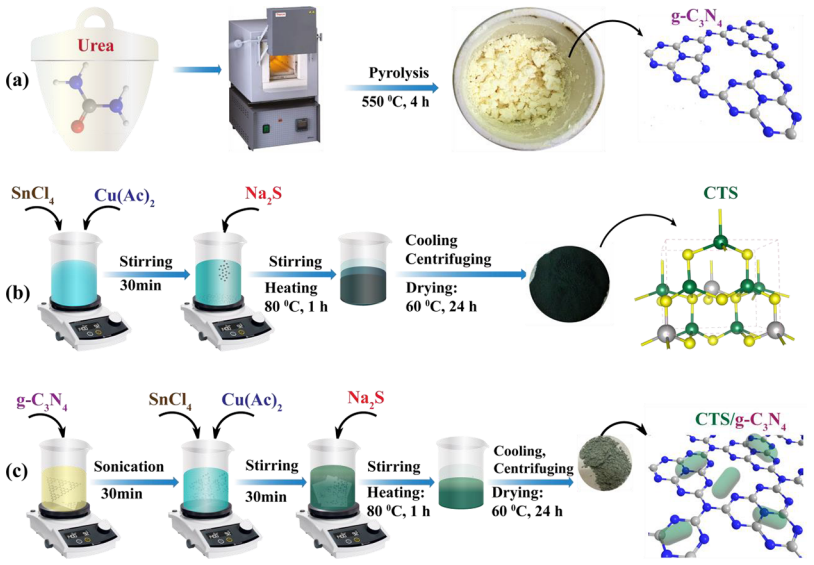

Figure 1. Schematics illustrating the synthesis of (a) CN, (b) CTS, and (c) CTS/CN composites.

X-ray diffractometer (Shimadzu, Japan) using Cu Kα radiation (λ = 0.15406 nm) operating at 40 kV, with 2θ ranging from 10° to 80° at a scanning rate of 3°/min. The surface morphology and elemental composition were determined from scanning electron microscopy (SEM) images taken on a Hitachi S4800 scanning electron microscope fitted with an EDS detector (Hitachi, Japan). High-resolution transmission electron microscopy (HRTEM) images of the samples were recorded on an FEI Tecnai F20 microscope with a beam energy of 300 kV (Thermo Fischer, USA). Nitrogen adsorption−desorption isotherms for analysis of the surface area and pore size were recorded with a Micromeritics ASAP-2020 instrument (Micromeritics Instrument Corporation, USA). The specific surface area was determined by the Brunauer−Emmett−Teller (BET) method. Pore size distributions were determined using the Barrett−Joyner−Halenda (BJH) method. XPS was performed on a Thermo ESCALAB 250 Xi XPS spectrometer (Thermo Scientific, USA) equipped with monochromatic Al Kα radiation (1486.6 eV), an X-ray source, and a hemispherical analyzer to determine the surface atomic composition and oxidation state. The optical properties and hence the bandgaps of the materials were determined from the absorption spectra recorded on an Azzota;, SM-1600 ultraviolet−visible spectrophotometer (Azzota Corp., USA). Photoluminescence (PL) measurements were carried out using an Agilent fluorescence spectrometer (Agilent, USA). Fourier transform infrared (FT-IR) spectra of the materials were recorded on a PerkinElmer FT-IR spectrometer (PerkinElmer, USA).

2.6. Electrochemical Characterization. Mott−Schottky, photocurrent, and electrochemical impedance spectroscopy (EIS) measurements for the determination of flat band potentials (E_{fb}) and charge-transfer resistance (R_{CT}) of the materials were carried out in a three-electrode system using an IVIUMSTAT potentiostat (Ivium Technologies, Netherlands). In the three-electrode system, Ag/AgCl was used as the reference electrode, platinum wire was used as the counter electrode, and a sample coated on an FTO substrate was used as the working electrode. The Mott−Schottky measurements were carried out in a 0.5 M aqueous Na_2SO_3 electrolyte in a potential range of −1.5 to +1.5 V, while EIS measurements were recorded in an electrolyte containing an aqueous solution of $K_4[Fe(CN)_6]$ and $K_3[Fe(CN)_4]$ in KCl. Transient photocurrent measurements were made in an aqueous Na_2SO_3 electrolyte using a 300 W tungsten halogen lamp to illuminate the working electrode. The light source was made on/off at 30 s intervals. The working electrodes were prepared by dispersing 50 mg of the synthesized material in DMF, depositing 20 μL of the mixture on a 1 cm^2 area of the FTO substrate, and drying it for 24 h in air.

2.7. Photocatalytic Activity Studies. The photocatalytic activities of the synthesized materials were evaluated by the degradation of the MO dye in an aqueous solution under visible light irradiation. The reaction was performed in a photochemical reactor using a 300 W tungsten halogen lamp (see Figure S6b). In a typical photocatalytic experiment, a 50 mg sample of the photocatalyst was added to 100 mL of a 15 mg/L aqueous solution of MO and stirred in the dark for 30 min using a magnetic stirrer. The mixture was then illuminated with visible light under continuous magnetic stirring for 120 min. To determine the rate of degradation of the dye, 3 mL samples were drawn from the reaction mixture at regular intervals of 30 min and centrifuged (4500 rpm for 10 min) to separate the photocatalyst. The concentration of the MO solution was then determined by measuring the absorbance at a wavelength of 464 nm with a UV−visible spectrophotometer. The photocatalytic degradation efficiency of the photocatalyst material was evaluated using the following eq:

$$\%D = \frac{(C_o - C)}{C_o} \times 100 \quad (1)$$

where $\%D$ is the percent degradation, C is the concentration of the dye after each irradiation time, and C_o is the initial concentration of the dye. A recyclability experiment for the best performing material was carried out for five cycles under conditions similar to those described above.

3. RESULTS AND DISCUSSION

3.1. Synthesis. The CN (g-C_3N_4) synthesized through the pyrolysis of urea is a fluffy lightweight powder with a pale-yellow color, while the CTS (Cu_3SnS_4) synthesized through the coprecipitation process is a black precipitate with a slight

https://doi.org/10.1021/acsomega.4c02414
ACS Omega 2024, 9, 28463−28475

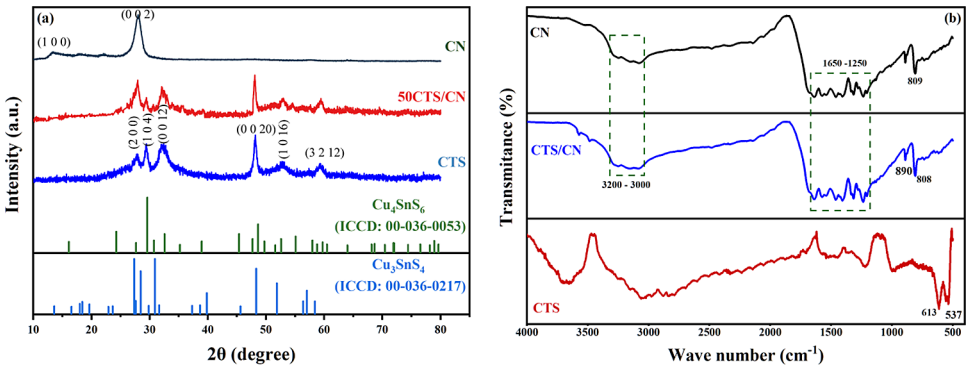

Figure 2. (a) Powder XRD patterns of CN, CTS, and 50CTS/CN with standard diffraction patterns of petrukite phase orthorhombic CTS and rhombohedral CTS. (b) FT-IR spectra of pristine CN, CTS, and the CTS/CN nanocomposite.

greenish tint and is insoluble in water. Schematics of the typical synthesis procedures for CN, CTS, and CN/CTS composites are illustrated in Figure 1a–c.

For the synthesis of the CTS/CN composites, a known amount of CN was added to a precursor solution used for the synthesis of CTS ($SnCl_4$ and $Cu(ac)_2$ dissolved in distilled water) and sonicated for 30 min, followed by precipitation with the addition of the precipitating agent. A series of CTS/CN composites with varying contents of CTS (20, 30, 40, 50, and 60% wt/wt). were prepared and labeled -20CTS/CN, 30CTS/CN, 40CTS/CN, 50CTS/CN, and 60CTS/CN. The purpose of preparing CTS/CN composites with different weight ratios of CTS was to optimize the bandgap.

3.2. Structure and Morphology. Figure 2a shows the powder XRD patterns of CN, CTS, and their composites. For pristine CN, two major peaks were observed at 2θ angles of 27.9° and 13.4°. The intense diffraction peak at 2θ = 27.9° has a *d*-spacing of 0.3183 nm and is assigned to the (0 0 2) reflection of a graphitic-like aromatic structure of CN. The relatively weak peak observed at 2θ = 13.4° with a *d*-spacing of 0.660 nm represents the (1 0 0) reflections of the in-plane repeating motifs of the continuous heptazine network. These two characteristic peaks are always assigned to CN and match well with those reported in the literature.[19,47] The XRD pattern for CTS (Figure 2a) revealed the existence of a mixed phase consisting of orthorhombic Cu_3SnS_4 and rhombohedral Cu_4SnS_6. The peaks at 2θ values of 27.3°, 48.2°, and 57° correspond to the (2 0 0), (0 0 20), and (3 2 12) diffraction planes, respectively, and can be indexed to petrukite, the *syn* phase of orthorhombic Cu_3SnS_4 (*ortho*-CTS) with a $Pmn2_1$ space group (ICDD: 00-036-0217).[33] The peaks at 2θ values of 29.6°, 32.5°, and 52.8° with the (1 0 4), (0 0 12), and (1 0 16) diffraction planes, respectively, can be indexed to rhombohedral Cu_4SnS_6 (*rhombo*-CTS) with the *R*3*m* space group (ICDD: 00-036-0053). The major peaks of both CN and CTS are observable in the XRD patterns of the CTS/CN composites, with no appreciable shift in position, indicating that the crystal structures of both CTS and CN were maintained during the synthesis process. The intensity of the (0 0 2) peak of CN decreased gradually with the increasing content of CTS in the composite.

To corroborate the existence of *ortho*-CTS and *rhombo*-CTS, density functional theory (DFT) calculations with the Perdew–Burke–Ernzerhof (PBE) exchange correlation function and ultrasoft pseudopotentials (UPPs) were used. Through DFT calculations, the crystal structures of both *ortho*- and *rhombo*-CTS were optimized and their XRD patterns were simulated. As shown in Figure S1, the simulated XRD patterns of the two crystal structures showed good agreement with the XRD patterns of the synthesized CTS sample, confirming the existence of a mixed phase.

The crystallite size (D) of the synthesized materials was calculated using the Scherrer equation (eq 2), where K is a constant (0.94), λ is the wavelength of the X-ray, β is the full width at half-maximum (fwhm), and θ is the diffraction angle. The calculations yielded average crystallite sizes of 6.51, 13.12, and 15.35 nm for CN, 50CTS/CN, and CTS, respectively, indicating a slight decrease in the size of the CTS/CN composite relative to that of pristine CTS.

$$D = K\lambda / \beta \cos\theta \tag{2}$$

The FT-IR spectra of the synthesized materials were recorded in the wavenumber range of 4000–500 cm^{-1} for the presence of functional groups and the structural conformation of CN. Figure 2b shows the FT-IR spectra of the CN, CTS, and CTS/CN composites. The peaks observed between 1200–1650 cm^{-1} are attributed to the stretching vibration modes of the C=N, C=C, and C–N functional groups in heptazine heterocycles, while the peak centered at around 3200 cm^{-1} is indicative of the N–H functional group and the adsorbed water molecules. Furthermore, the typical peak at 809 cm^{-1} is indicative of the presence of the *s*-triazine ring unit, while the absorption band at 890 cm^{-1} corresponds to the deformation mode of the N–H bond. These findings are consistent with values reported for CN in other studies.[44,48] For pristine CTS, the peaks around at 540 and 669 cm^{-1} could be attributed to the vibration of the Sn–S bond,[49,50] while the peak centered around 613 cm^{-1} is due to the vibrational mode of the Cu–S bond.[50,51] It could also be observed that the characteristic peaks of CN appeared in CTS/CN composites, but the characteristic peak due to the *s*-triazine ring vibration of CN nanosheets (at 809 cm^{-1}) is shifted to 808 cm^{-1} for the composite, indicating the possibility of interactions between CN and CTS in the composite.[52]

SEM and transmission electron microscopy (TEM) imaging techniques were used to elucidate the morphological and microstructural features of the CN, CTS, and 50CTS/CN composites. The corresponding SEM images shown in Figure 3a–c revealed that the pristine CTS exhibited nanoplate-like morphology with some degree of agglomeration of plates (see inset of Figure 3a), while pristine CN shows thin sheet-like morphology wrinkled and folded at the edges. For the CTS/

https://doi.org/10.1021/acsomega.4c02414
ACS Omega 2024, 9, 28463–28475

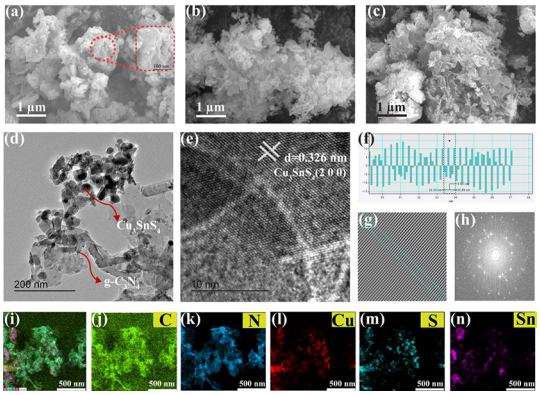

Figure 3. SEM images of (a) pristine CTS, (b) pristine CN, (c) 50CTS/CN composite, (d) TEM image, (e–h) HRTEM image and IFFT profile, and (i–n) STEM-EDS elemental mapping images of the 50CTS/CN composite.

CN composite, the CTS nanoplates were deposited on the slightly exfoliated CN nanosheets (Figure 3c,d).

Figure 3d,e shows low- and high-resolution TEM images of the 50CTS/CN composite. The TEM and HRTEM images show the presence of CTS NPs on the CN sheet, with a lattice-fringe *d*-spacing of 0.326 nm which is indexed to the (2 0 0) reflection plane of orthorhombic CTS. The results are also consistent with *d*-spacing values reported in the XRD results. Figure 3f–h represents FFT and IFFT images of Figure 3e generated by Gatan software used for the estimation of *d*-spacing values of CTS. Moreover, the surface compositions and distributions of the elements in the 50CTS/CN composite were determined through energy-dispersive X-ray (EDS) elemental mapping technique carried out along SEM and TEM characterizations (see Figure S2 for SEM-EDS elemental maps). As shown in Figure 3i–n, the STEM-EDS elemental maps of the 50CTS/CN composite showed the existence of the elements Cu, S, Sn, C, and N with a uniform distribution on the surface, as also evidenced by the existence of the CTS NPs on the surface of CN, as shown in the TEM image depicted in Figure 3d. In addition, the intimate contact between the CN and CTS nanoparticles is clearly observed in Figures 3d and S3, which could favor the formation of a junction between the two semiconductors, thus improving the charge separation and therefore the photocatalytic activity.

3.3. Oxidation States and Composition. The surface elemental composition and oxidation state of elements in the 50CTS/CN composite were analyzed through the XPS characterization technique. Figure 4 presents the survey XPS spectra along with high-resolution core-level spectra of Cu, Sn, S, C, and N. The survey spectrum displayed in Figure 4a demonstrates the existence of elements Cu, Sn, S, C, and N in the composite, which is consistent with the EDS results. Figure 4b depicts a high-resolution Cu 2p core-level spectrum depicting the Cu $2p_{3/2}$ and Cu $2p_{1/2}$ core levels. The two Cu 2p peaks are doublets and can be deconvoluted into two separate peaks, representing the existence of both Cu^{+} and Cu^{2+} species in CTS, as reported in other works.[37] The peaks centered at 932.0 and 952.0 eV correspond to Cu^{+}, whereas the peaks centered at 933.5 and 953 eV of the corresponding core levels indicate the existence of Cu^{2+}.[34,53] Besides, the satellite peak centered at 942.8 eV also belongs to Cu^{2+}, signifying the existence of both Cu^{+} and Cu^{2+} states in CTS.[34,54−56] Moreover, since Cu_3SnS_4 is a charge neutral compound, it should have Cu in both Cu^{+} and Cu^{2+} states, and the formula expressed as $(Cu^{+})_2Cu^{2+}Sn^{4+}(S^{2-})_4$. Figure 4c displays a high-resolution XPS spectrum of the Sn 3d state. The two strong peaks centered at around 487.2 and 495.65 eV with splitting of 8.5 eV correspond to Sn $3d_{5/2}$ and $3d_{3/2}$ core levels, respectively, indicating the existence of Sn^{4+}.[34,53] The S 2p core-level spectrum shown in Figure 4d displays two peaks centered at 162.7 and 169.4 eV. The peak centered around 162 eV corresponds to the 2p core-level, confirming the existence of sulfur in the S^{2-} state.[34,53] The additional peak centered at 169.4 eV represents S in SO_4^{2-}, most likely formed due to the oxidation of sulfur by oxygen adsorbed to the surface.[57] Thus, the XPS analysis of CTS reveals the existence of the elements Cu, Sn, and S in the oxidation states of Cu^{+}, Cu^{2+}, Sn^{4+}, and S^{2-}.[37]

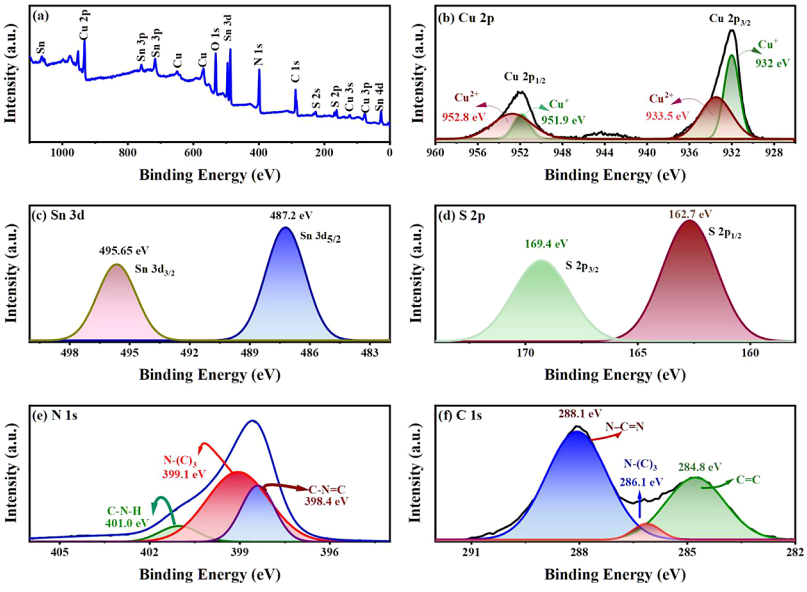

Figure 4. XPS spectra of 50CTS/CN composite: (a) survey, (b) Cu 2p, (c) Sn 3d, (d) S 2p, (e) N 1s, and (f) C 1s.

https://doi.org/10.1021/acsomega.4c02414
ACS Omega 2024, 9, 28463−28475

For the CN, the C 1s spectra in Figure 4f show two major peaks centered around 288 and 284 eV. When deconvoluted, they resolve into three peaks centered at 288.1, 284.8, and 286.1 eV, representing carbon in three different environments. The major peak centered at 288.1 eV is attributed to sp^2-bonded carbon (N−C=N), and the other peaks centered at 286.1 and 284.8 eV represent C in C−NH_2 and C=C bonds, respectively, which are usually observed on the XPS spectra of CN.[19,47] These findings are consistent with the three types of carbons in CN elucidated in the FT-IR analysis. The deconvoluted high-resolution N 1s spectra depicted in Figure 4e reveal three distinct peaks centered at 398.4, 399.1, and 401.0 eV. The peak centered at 398.4 eV belongs to sp^2 hybridized aromatic nitrogen bonded to carbon (C−N=C). The peak centered at 399.1 eV is assigned to the nitrogen in N−$(C)_3$, while the weak peak with a binding energy of 401.0 eV corresponds to the N in C−N−H.[19,47]

3.4. Surface Area Analysis. To understand the adsorption capability of the synthesized materials, the surface areas and distribution of pore size of the synthesized materials, including pristine CTS, CN, and 50CTS/CN, were determined based on the N_2 gas adsorption−desorption isotherm measured at a temperature of 77 K. The Brunauer−Emmett−Teller (BET) method was employed to calculate specific surface areas, while the Barret−Joyner−Halender (BJH) method was used to determine the pore size distribution and pore volume. As shown in Figure S4, the materials displayed a type IV isotherm with an H_4 hysteresis loop, which is indicative of the existence of mesopores.[21] The average pore size and cumulative pore volumes of the synthesized materials were determined from the BHJ desorption data. The pore size distribution graph (inset of Figure S4) shows a range of pore size distribution extending from 2−123 nm, further confirming the presence of mesopores and macropores, especially in CTS and 50CTS/CN composite material, which can also be evidenced by the higher adsorption observed around the relative pressure (P/P_0) range close to 1.[31]

The calculated BET surface areas (S_{BET}) and pore parameters of CTS, CN, and 50CTS/CN are presented in Table 1. The data show that CN exhibited the highest BET surface area and pore volume of 56.76 m^2/g and 0.399 cm^3/g, respectively, followed by 50CTS/CN (36.37 m^2/g, 0.0166 cm^3/g) and CTS (8.09 m^2/g, 0.063 cm^3/g). The highest specific surface area of CN can be attributed to its porous sheet-like morphology, which is consistent with SEM findings. In terms of the pore size, CN displayed the highest average pore size which is due to the existence of macropores. The incorporation of CTS into CN decreased the surface area of CN due to the coverage of holes in CN by the CTS NPs.

Table 1. BET Specific Surface Area, Average Pore Size, and Pore Volume of CN, 50CTS/CN, and CTS Materials

material	S_{BET} (m^2/g)	average pore size (nm)	pore volume (cm^3/g)
CN	56.76	32.37	0.3995
50CTS/CN	36.37	13.67	0.166
CTS	8.09	26.89	0.063

In addition to surface area, the adsorptive capacity of a photocatalyst is also dependent on the surface charge. The surface charge of a catalyst material is dependent on the maturity of the material and the pH of the sample solution. Accordingly, to get insight into the surface charge exhibited by the photocatalyst, the pH of the point of zero charge (PZC) was determined as described elsewhere.[58] As shown in Figure S5, the results revealed pH(PZC) values of 5.54, 5.28, and 6.2 for CN, CTS, and 50CTS/CN composite material, respectively, revealing the observed improved adsorption of MO dye by CTS and 50CTS/CN (see Figure 8a).

3.5. Optical Properties. Figure 5 depicts the UV−visible absorption spectrum of the synthesized CN, CTS, and 50CTS/CN composite. In the pristine CN (Figure 5a), the absorption maxima is centered at 322 nm and an absorption edge around 451 nm, suggesting that CN is not efficient in utilizing the whole visible light spectrum.[44] Meanwhile the CTS material exhibits absorption in the UV−visible range, and further extends into the near-infrared, with an absorption edge around 726 nm, suggesting that this material is efficient in utilizing the full solar spectrum (Figure 5c). As shown in Figure 5b, the CTS/CN composite has absorption maxima red-shifted to a longer wavelength, relative to the pristine CN leading to a broadened light absorption range and hence a narrower bandgap for the composite. It can be concluded that the synergetic effect between CN and CTS allowed the composite materials to absorb light more efficiently and maximize visible light utilization. This trend was also observed for composites involving CN and transition-metal sulfides.[20,38,59]

The bandgaps of the synthesized materials were determined from the UV−vis absorption spectra by employing Tauc equation (eq 3) and plotting $(\alpha h\nu)^n$ vs $h\nu$ through extrapolation of the linear region of the plot to the x-intercept.

$$(\alpha h\nu)^n = A(h\nu - E_g) \tag{3}$$

where α, h, ν, and A represent the absorption coefficient, the Planck constant, the frequency of light absorbed, and a constant, respectively. The value of n depends on the type of optical transition.[27] As shown in Tauc's plots (insets of Figure

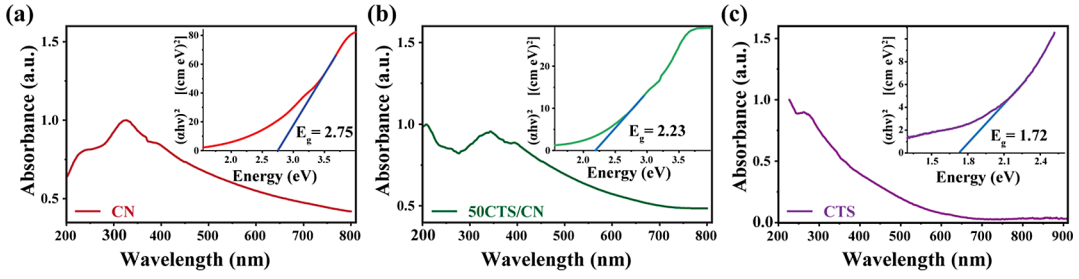

Figure 5. Ultraviolet−visible absorption spectra of (a) CN, (b) 50CTS/CN, and (c) CTS materials with insets of Tauc plots and the estimated bandgaps.

https://doi.org/10.1021/acsomega.4c02414
ACS Omega 2024, 9, 28463−28475

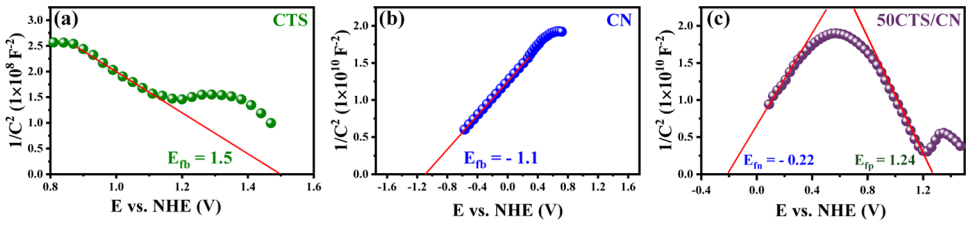

Figure 6. MS plots of (a) CTS, (b) CN, and (c) 50CTS/CN composite obtained from EIS measurements carried out at 100 Hz.

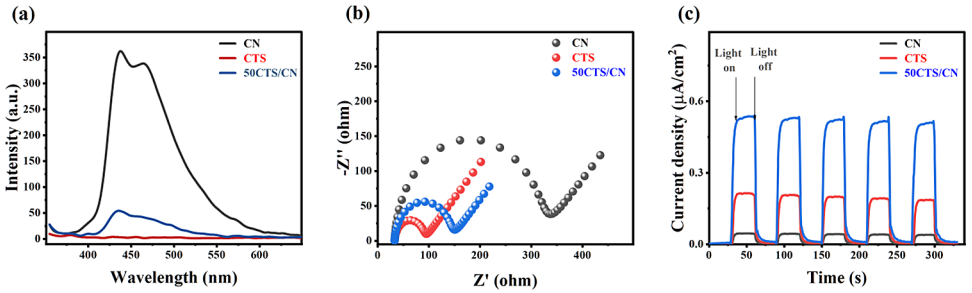

Figure 7. (a) PL spectra, (b) transient photocurrent response, and (c) EIS Nyquist plot of CN, CTS, and 50CTS/CN composite samples, respectively.

5a−c), the bandgap (E_g) values of CTS, 50CTS/CN, and CN were calculated to be 1.72, 2.23, and 2.75 eV, respectively. The obtained bandgap values agree with those reported elsewhere for both CN[44,48] and CTS.[35,37,60,61] Along with bandgaps, the conduction band potential (E_{CB}) and valence band potentials (E_{VB}) of CTS and CN were calculated via Mulliken electronegativity theory using eqs 4 and 5, where E_{CB}, E_{VB}, E_e, χ, and E_g refer to the conduction band potential, valence band potential, energy of free electrons on the hydrogen scale (4.5 eV), absolute electronegativity, and bandgap energy of the materials, respectively. The χ in eq 4 is the Mulliken electronegativity of the semiconductor, which can be obtained by taking the geometric mean of the Mulliken electronegativity of constituent atoms in the semiconductor. The χ of an atom is the arithmetic mean of its electron affinity and the first ionization energy.[32,62]

$$E_{CB} = \chi - E_C - 0.5E_g \quad (4)$$

$$E_{VB} = E_{CB} - E_g \quad (5)$$

Using E_g values determined from UV−visible absorption spectra and χ values reported in the literature: 5.16 eV for CTS[63] and 4.63 eV[64] for CN; an E_{CB} value of −0.20 eV and E_{VB} of 1.52 eV were obtained for CTS, while for CN, E_{CB} and E_{VB} were calculated to be −1.25 and 1.50 eV, respectively.

Mott−Schottky (MS) measurements were also made to determine the type of conductivity (p- or n-type) exhibited by the synthesized materials, analyze their energy band structure, and the formation of a p−n heterojunction to understand the photocatalytic mechanism involved. As shown in Figure 6a, the slope of the plot of the linear part of the MS curve of CTS is negative, indicating p-type semiconductivity,[61,65] while a positive slope for CN confirmed n-type semiconducting behavior (Figure 6b). Besides, the band edge potentials of the synthesized materials were estimated from the flat band potentials (E_{fb}) obtained from the MS plots by extrapolating the linear portion of the plot of $1/C^2$ vs potential to the x-intercept (where $1/C^2 = 0$). Accordingly, the flat band potentials of CN and CTS were estimated to be −1.1 and +1.5 V, respectively, relative to the normal hydrogen electrode (NHE). Studies[27] have shown that for an n-type semiconductor, the E_{CB} is 0.1 V lower than the E_{fb}, while E_{VB} of a p-type semiconductor is 0.1 V higher than the E_{fb}, resulting in E_{CB} of −1.2 V for CN and E_{VB} of 1.6 V for CTS. These values are close to the band edge values calculated using eq 4 based on Mulliken electronegativity theory[62] as summarized in Table S1.

Besides, as shown in Figure 6c, the MS plot of the 50CTS/CN composite has an inverted V-shape with positive and negative slopes, representing the n-type CN and p-type CTS, revealing the formation of a p−n heterojunction. It can be seen that, in the CTS/CN composite, the E_{fb} of CTS shifted upward to a less positive value (+1.24 V vs NHE) while that of CN shifted downward (−0.22 V vs NHE) along with the CB and VB positions relative to the pristine materials, resulting in the directional migration of photoinduced electrons from CB of CTS to CB of CN and photoinduced holes from VB of CN to VB of CTS, leading to enhanced charge separation. This finding is consistent with those reported for composites made of n- and p-type materials.[25−27]

3.6. Extent of Carrier Separation and Transfer Properties. Photocurrent, photoluminescence (PL), and EIS measurements were used to understand the extent of carrier generation, separation, and transfer among the synthesized materials. PL measurements were employed to investigate the extent of the carrier separation efficiency of the semiconductor photocatalyst. The extent of carrier separation efficiency among the catalysts is usually related to the intensity of the PL emission peak, as it is related to carrier recombination. Figure 7a shows the PL spectra of the CN, CTS, and CTS/CN composites obtained with an excitation wavelength of 340 nm. As shown, CN and the CTS/CN composites displayed PL emission peaks in the wavelength range of 434−438 nm, with the pristine CN showing the most intense peak, revealing a higher carrier recombination rate. Compared to the pristine CN, the dramatic drop in the PL emission intensity of the 50CTS/CN composite reveals an enhancement in carrier separation efficiency because of suppression of carrier

https://doi.org/10.1021/acsomega.4c02414
ACS Omega 2024, 9, 28463−28475

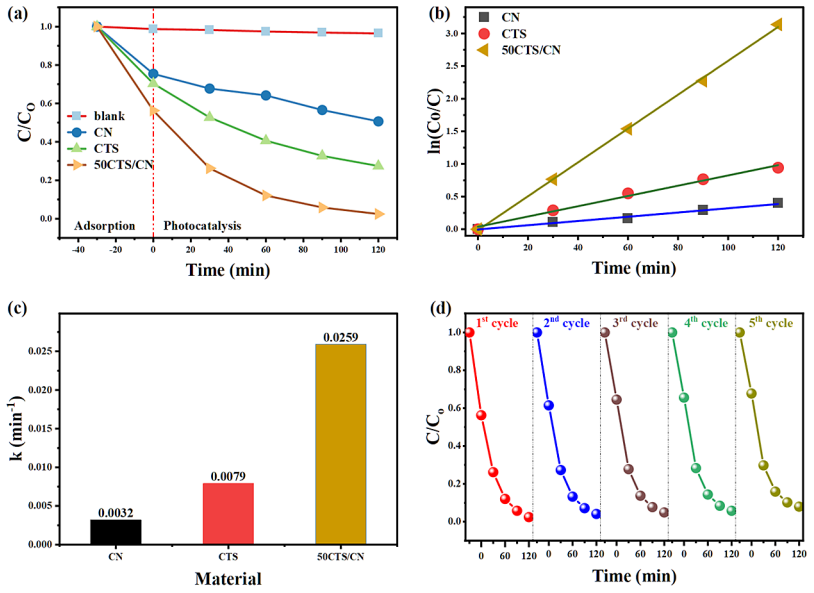

Figure 8. (a) Adsorption and photocatalytic degradation of MO over the synthesized materials under visible light irradiation; (b) pseudo-first-order kinetic fitting of the photodegradation of MO; (c) fitted pseudo-first-order kinetic constants for MO photodegradation; and (d) stability test of 50CTS/CN for MO photodegradation.

recombination, which could be favorable for improved photocatalytic activity. This could be attributed to the migration of the photogenerated electron−hole pairs between CTS and CN as a result of the formation of a p−n heterojunction.

EIS measurements were also performed to understand the extent of the charge-transfer resistance at the interface between the electrolyte and the working electrode. The extent of charge-transfer resistance (R_{CT}) can be inferred from the radius of the semicircle in the high-frequency region of the EIS Nyquist plot. Figure 7b depicts Nyquist plots of EIS measurements recorded at a frequency of 100 Hz. The results of the EIS measurement showed that the 50CTS/CN composite exhibited better charge transfer efficiency than that of pristine CN, as evidenced by the significantly smaller semicircle compared to that of pristine CN. Additionally, the results of the photocurrent studies depicted in Figure 7c showed that the light-on photocurrent of the 50CTS/CN composite was found to be 2.4 and 11 times higher than that of pristine CTS and CN, respectively. The result demonstrated the improved separation and transport of photogenerated charge carriers due to the existence of a p−n heterojunction at the interface between CTS and CN.

3.7. Photocatalytic Activity. The performances of the synthesized materials were evaluated for the degradation of the MO dye in an aqueous solution under irradiation by visible light. The pristine CN, CTS, and CTS/CN composites were evaluated for visible light-induced degradation of the MO dye. A small amount of H_2O_2 (100 μL) was added to the reaction mixture to initiate the degradation of MO.[20,35,66] Before irradiation, to establish the dark adsorption equilibrium, the adsorption of the 5OCTS/CN composite in the dark was recorded. As shown in Figure S7, the composite material exhibited a good adsorption capability, and the dark adsorption equilibrium was established after 30 min.

The progress of degradation of MO dye over time was monitored by measuring the UV−visible absorption (at λ = 464 nm) of the reaction mixture removed from the reactor at a predefined time interval (30 min) as the reaction progressed. As shown in Figure S6a, the absorption peaks of the MO dye decreased gradually as the reaction progressed, indicating the degradation of the MO dye. Figure 8a displays the progress of the removal of MO by the synthesized materials through adsorption and photocatalysis. The results revealed that all the CTS/CN composites exhibited enhanced performance relative to either the pristine CN or CTS. For the pristine CTS and CN, only 60.99 and 32.8% of MO were degraded after irradiation for 120 min. In contrast, all the CTS/CN nanocomposites displayed improved activity (higher than that of both CN and CTS), with the 50CTS/CN composite displaying a 95.6% degradation efficiency (Figure S6c,d).

As shown in Figure 8b, the photocatalytic reaction was found to fit with pseudo-first-order kinetics ($\ln(C_0/C) = kt$) with $R^2 > 0.99$, where C represents the concentration of MO at any time, t, during the reaction, C_o represents the initial concentration of the dye, and k represents the rate constant of the reaction. The corresponding slope of the linear fit plot of $\ln(C_0/C)$ vs kt represents the value of the rate constant, k. The calculated pseudo-first-order kinetic rate constants of CN, CTS, and 50CTS/CN were 0.0032, 0.0079, and 0.0259 min^{-1}, respectively (see Figure 8c). The rate of reaction for the 50CTS/CN composite photocatalyst was found to be 3.28 and 8 times that of pristine CTS and CN, respectively, showing enhanced performance of the 50CTS/CN composite over either the pristine CN or CTS.

The stability/reusability of the CTS/CN composite photocatalyst was tested by employing it for five consecutive photodegradation reaction cycles. The results displayed in Figure 8d showed that after five cycles of use, the photocatalyst retained 92.2% of its initial capacity, indicating the good stability and reusability of the photocatalyst. XRD analysis of the 50CTS/CN composite was carried out after its usage for 5 consecutive cycles. As shown in Figure S8b, the XRD pattern of the used 50CTS/CN composite revealed that the phase and structure remain intact. These results indicated that the heterostructure composite photocatalyst is sufficiently stable

https://doi.org/10.1021/acsomega.4c02414
ACS Omega 2024, 9, 28463−28475

Table 2. Comparison of Photocatalytic Degradation of MO by Various CTS-Based and Other Types of Materials

material	[MO] (mg/L)	catalyst dosage (mg)	removal efficiency, % (min)	ref
CN/$NiFe_2O_4$	10	24	CN:53 (210) $NiFe_2O_4$:32(210) CN/$NiFe_2O_4$: 100 (210)	21
CN-@NiAl-LDH			99 (180)	24
CN/α-Fe_2O_3	100	10	CN:41 (300) α-Fe_2O_3:30 (300) CN/α-Fe_2O_3:97 (300)	23
CN/TiO_2	20	100	TiO_2:46 (80) CN:28 (80) CN/TiO_2:97 (80)	67
Cu_2SnS_3	5	50	Cu_2SnS_3:80 (240)	41
CTS/rGO	20	20	CTS:82 (120) CTS/rGO:97 (120)	35
Cu_2SnS_3/rGO	10	50	Cu_2SnS_3:57.3 (180) Cu_2SnS_3/rGO:94.3 (180)	40
CTS/CN	20	50	CTS:60.99 (120) CN:32.8 (120) CTS/CN:95.6 (120)	this work

during the photodegradation of MO dye. Compared to other related studies involving CN, CTS, and related materials for visible light-induced degradation of MO, the composite material reported in this work performed well. A summary of the photocatalytic performance of various materials for MO degradation reported in this study, along with similar materials reported in other studies,[21,23,24,35,40,41,67] is presented in Table 2.

The enhanced photocatalytic performance of the composite can be ascribed to the optimized bandgap that led to broadening of the light absorption range, efficient charge separation, and transfer at the interface between CTS and CN due to the formation of a p−n hetrojunction. The improved charge separation (decreased charge recombination rate) of the composite catalyst was demonstrated from the decreased intensity of the PL emission peaks of the pristine CN after forming composites with CTS. Furthermore, EIS and photocurrent results revealed improved photoinduced charge generation, separation, and transfer for the composite as compared to either of pristine CTS or CN.

3.8. Mechanism behind the Improved Photocatalytic Performance. A photocatalytic process mainly depends on the excellent charge separation efficiency, smooth transfer of photoinduced charge carriers within the semiconductor, and suitable band edge positions of the photocatalyst. From the results of UV−visible and MS measurements discussed earlier, the Fermi level and the band edge positions of CN were higher than those of CTS before contact. After contact, a p−n heterojunction was formed between p-CTS and n-CN. As a result, electrons migrated from the CB of CN toward the CB of CTS, while hole transfer occurred from the VB of CTS to the VB of CN, leading to the accumulation of negative charge on CTS and positive charge on CN. The accumulation of electrons over CTS could raise the Fermi level of CTS and lower the Fermi level of CN, along with the band edge potentials in the CTS/CN composite.[26] The MS measurements for the CTS/CN composite have confirmed the formation of a p−n heterojunction between CTS and CN (Figure 6c), which resulted in the shift of the band edge potentials of both p-CTS and n-CN until the Fermi level equilibrium was reached through band bending. This resulted in E_{VB} of 1.24 eV and E_{CB} of −0.48 eV for CTS and E_{VB} of 2.53 eV and E_{CB} of −0.22 eV for CN, leading to the directional flow of photoinduced electrons from the CB of CTS toward the CB of CN and photoinduced holes from the VB of CN to the VB of CTS, effectively preventing the recombination of the charge carriers along with the internal electric field established across the junction due to the spontaneous diffusion of electrons and holes near the interface between CTS and CN. Figure 9 depicts the energy band schematic diagram for p-CTS and n-type CN before and after contact.

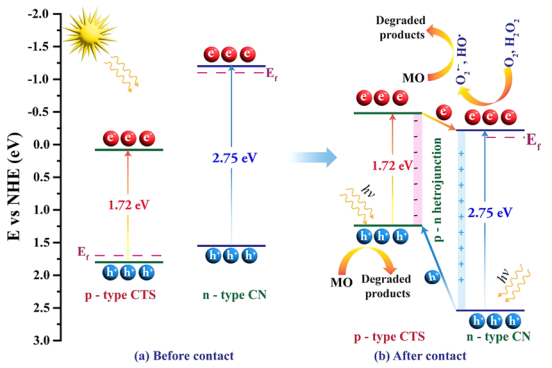

Figure 9. Schematics illustrating the possible charge transfer mechanism before and after contact for enhanced photocatalytic degradation of MO by a p−n heterojunction CTS/CN composite photocatalyst.

With visible light illumination, both CTS and CN could be excited to generate photoinduced electron (e^-)−hole (h^+) pairs (eq 6). Due to a more negative CB of CTS, the photoinduced electrons on the CB of CTS migrate toward the CB of CN, while photoexcited holes migrate from the higher VB potential of CN toward the lower VB potential of CTS. As the E_{CB} of CN (−0.22 V vs NHE) is more negative than the standard redox potential of the $O_2/O_2^{\cdot-}$ (−0.18 V vs NHE),[58] the photoinduced electrons that accumulate on the CB of CN will be captured by O_2 to yield peroxide radical ($O_2^{\cdot-}$) and hydroxy radical (HO$^{\cdot}$) through eqs 7−9. Meanwhile, as the VB potential of CN is more positive than the $HO^-/HO^{\cdot}$ couple (1.90 V vs NHE),[58] the photoinduced holes on the VB of CN will trap the surface attached HO^- to form HO$^{\cdot}$ through eq 10. The generated $O_2^{\cdot-}$ and HO$^{\cdot}$ radicals would thus participate in the oxidative degradation of MO dye as depicted in eqs 11 and 13. Besides, as the redox potential of MO (0.955 V vs NHE)[58] is lower than the E_{VB} of both CTS and CN, photoinduced holes on the VB of CTS and CN can directly attack and degrade the MO dye (eq 12). To further confirm the proposed mechanism, the primary reactive species involved in the photodegradation of the MO dye were explored through scavenger experiments conducted by introducing isopropyl alcohol (IPA), benzoquinone (BQ), and EDTA to the reaction mixture as scavengers for hydroxyl radicals (HO$^{\cdot}$), superoxide radicals ($O_2^{\cdot-}$), and hole species (h^+), respectively. As shown in Figure S8a, the addition of the hole scavenger EDTA suppressed the degradation of MO strongly followed by BQ. However, with the addition of the HO$^{\cdot}$ scavenger, IPA, the degradation of MO was only slightly depressed, suggesting h^+ and $O_2^{\cdot-}$ as the major reactive species responsible for the degradation of MO dye.[21,22,68]

$$\text{CTS/CN} + h\nu \rightarrow e^- + h^+ \quad (6)$$

https://doi.org/10.1021/acsomega.4c02414
ACS Omega 2024, 9, 28463−28475

$$O_2 + e^- \rightarrow O_2^{\cdot -} \quad (7)$$

$$O_2^{\cdot -} + 2H^+ \rightarrow H_2O_2 \quad (8)$$

$$H_2O_2 + O_2^{\cdot -} \rightarrow HO^- + HO^{\cdot} + O_2 \quad (9)$$

$$HO^- + h^+ \rightarrow HO^{\cdot} \quad (10)$$

$$MO + O_2^{\cdot -} \rightarrow \text{degraded products} \quad (11)$$

$$MO + h^+ \rightarrow \text{degraded products} \quad (12)$$

$$MO + HO^{\cdot} \rightarrow \text{degraded products} \quad (13)$$

4. CONCLUSIONS

A novel p−n heterojunction copper tin sulfide/graphite carbon nitride (CTS/CN) nanocomposite along with the pristine CTS and CN were successfully synthesized through pyrolysis and a simple coprecipitation method and evaluated for the photocatalytic degradation of an aqueous solution of MO dye under visible light illumination. Characterization results showed that CTS nanoplates were dispersed on the wrinkled sheet-like surface of CN. Among the composites, the 50CTS/CN composite displayed the highest photocatalytic efficiency of 95.6% for the degradation of MO dye under visible light illumination for 120 min, which is 2.9 times that of pristine CN. This enhanced performance exhibited by the 50CTS/CN composite could be attributed to the extended and improved visible light absorption range due to the optimized bandgap; enhancement in carrier separation efficiency due to the formation of a p−n heterojunction; and efficient transport of photogenerated electron−hole pairs as evidenced by PL, photocurrent, and EIS results. Recyclability studies also showed high photostability and activity, where the 50CTS/CN composite retained 92.2% of its initial capacity after five consecutive runs, showing its potential for the removal of the MO dye from an aqueous solution. The results of this study showed that the CTS/CN composite is a stable and efficient promising visible light responsive photocatalytic material for the removal of MO and other toxic dyes.

■ ASSOCIATED CONTENT

Supporting Information

The Supporting Information is available free of charge at https://pubs.acs.org/doi/10.1021/acsomega.4c02414.

SEM/EDS elemental maps of the 50CTS/CN composite; nitrogen adsorption−desorption isotherms with the inset showing the corresponding pore size distribution curves of the CTS, CN, and 50CTS/CN samples; photocatalytic activity of the synthesized materials expressed as a plot of C/C_0, $C_0 - C/C_0$, images of the MO solutions at different stages of the photocatalysis process, and image of the photoreactor used for the photocatalytic process; crystal structure of orthorhombic Cu_3SnS_4, rhombohedral Cu_4SnS_6, XRD spectra of synthesized CTS, and simulated XRD patterns of DFT optimized crystal structures of orthorhombic Cu_3SnS_4, and rhombohedral Cu_4SnS_6 with detailed description of DFT calculations; trapping experiment of active species during the photocatalytic degradation of MO over 50CTS/CN composite under visible light irradiation; XRD patterns of the 50CTS/CN heterojunction composite before and after 5-cycle of reuse; comparison of valence and conduction band edges estimated based on Mullikan's electronegativity theory and Mott−Schottky measurements; adsorption MO dye by 50CTS/CN composite in the dark recorded for 90 min; determination of pH of point of zero charge; and HRTEM image showing junction formation between the CTS and CN in the CTS/CN composite (PDF)

■ AUTHOR INFORMATION

Corresponding Authors

Lemma Teshome Tufa − *Department of Applied Chemistry, Adama Science and Technology University, Adama 1888, Ethiopia; Research Institute of Materials Chemistry, Chungnam National University, Daejeon 34134, Republic of Korea;* orcid.org/0000-0001-6929-8464; Email: lemmat2003@yahoo.com

Jaebeom Lee − *Department of Chemistry and Research Institute of Materials Chemistry, Chungnam National University, Daejeon 34134, Republic of Korea;* orcid.org/0000-0002-8414-7290; Email: nanoleelab@cnu.ac.kr

Authors

Endale Kebede Feyie − *Department of Applied Chemistry, Adama Science and Technology University, Adama 1888, Ethiopia;* Present Address: Department of Chemistry, Dire Dawa University, P.O. Box: 1362, Dire Dawa, Ethiopia; orcid.org/0000-0001-7461-0707

Enyew Amare Zereffa − *Department of Applied Chemistry, Adama Science and Technology University, Adama 1888, Ethiopia*

Aschalew Tadesse − *Department of Applied Chemistry, Adama Science and Technology University, Adama 1888, Ethiopia;* orcid.org/0000-0001-6962-1479

Mahendra Goddati − *Department of Chemistry, Chungnam National University, Daejeon 34134, Republic of Korea;* orcid.org/0000-0003-2743-1954

Daegwon Noh − *Department of Physics, Chungnam National University, Daejeon 34134, Republic of Korea; Institute of Quantum Systems (IQS), Chungnam National University, Daejeon 34134, Korea*

Eunsoon Oh − *Department of Physics, Chungnam National University, Daejeon 34134, Republic of Korea; Institute of Quantum Systems (IQS), Chungnam National University, Daejeon 34134, Korea*

Complete contact information is available at: https://pubs.acs.org/10.1021/acsomega.4c02414

Author Contributions

The manuscript was written through the contributions of all authors. All authors have approved the final version of the manuscript.

Notes

The authors declare no competing financial interest.

■ ACKNOWLEDGMENTS

The authors would like to thank the Postgraduate Program of Adama Science and Technology University (ASTU/AS-R/013/2021) and Dire Dawa University, Dire Dawa, Ethiopia, for financially supporting this research. This research was also supported by the National Research Foundation of Korea (NRF), grant funded by the Korean government (MSIT) number RS-2023-00219710; Industrial Strategic Technology

Development Program, grant number 20025720, funded by the Ministry of trade, Industry & Energy (MOTIE, Korea); the Brain Pool program funded by the Ministry of Science and ICT through the National Research Foundation of Korea (NRF-2021H1D3A2A01099457, 2022H1D3A2A01093556).

REFERENCES

(1) Peerakiatkhajohn, P.; Butburee, T.; Sul, J.; Thaweesak, S.; Yun, J.-H. Efficient and Rapid Photocatalytic Degradation of Methyl Orange Dye Using Al/ZnO Nanoparticles. *Nanomaterials* **2021**, *11* (4), 1059.

(2) Abass, A. K.; Raoof, S. D. Advanced Oxidation Process Treatment for Azo Dyes Pollutants Using Ultra-Violet Irradiation. *J. Phys. Conf. Ser.* **2020**, *1664*, No. 012066.

(3) Sen, S. K.; Raut, S.; Bandyopadhyay, P.; Raut, S. Fungal Decolouration and Degradation of Azo Dyes: A Review. *Fungal Biol. Rev.* **2016**, *30* (3), 112−133.

(4) Balakrishnan, V. K.; Shirin, S.; Aman, A. M.; de Solla, S. R.; Mathieu-Denoncourt, J.; Langlois, V. S. Genotoxic and Carcinogenic Products Arising from Reductive Transformations of the Azo Dye, Disperse Yellow 7. *Chemosphere* **2016**, *146*, 206−215.

(5) Bhattacharya, P.; Swarnakar, S.; Ghosh, S.; Majumdar, S.; Banerjee, S. Disinfection of Drinking Water via Algae Mediated Green Synthesized Copper Oxide Nanoparticles and Its Toxicity Evaluation. *J. Environ. Chem. Eng.* **2019**, *7* (1), No. 102867.

(6) Safavi-Mirmahalleh, S.-A.; Salami-Kalajahi, M.; Roghani-Mamaqani, H. Adsorption Kinetics of Methyl Orange from Water by PH-Sensitive Poly(2-(Dimethylamino)Ethyl Methacrylate)/Nanocrystalline Cellulose Hydrogels. *Environ. Sci. Pollut. Res.* **2020**, *27* (22), 28091−28103.

(7) Neethu, N.; Choudhury, T. Treatment of Methylene Blue and Methyl Orange Dyes in Wastewater by Grafted Titania Pillared Clay Membranes. *Recent Pat. Nanotechnol.* **2018**, *12* (3), 200−207.

(8) Al-Baldawi, I. A.; Abdullah, S. R. S.; Almansoory, A. F.; Ismail, N. I.; Hasan, H. A.; Anuar, N. Role of Salvinia Molesta in Biodecol_orization of Methyl Orange Dye from Water. *Sci. Rep.* **2020**, *10*, 13980.

(9) Liu, J.; Peng, G.; Jing, X.; Yi, Z. Treatment of Methyl Orange by the Catalytic Wet Peroxide Oxidation Process in Batch and Continuous Fixed Bed Reactors Using Fe-Impregnated 13X as Catalyst. *Water Sci. Technol.* **2018**, *78* (4), 936−946.

(10) Garrido-Cardenas, J. A.; Esteban-García, B.; Agüera, A.; Sánchez-Pérez, J. A.; Manzano-Agugliaro, F. Wastewater Treatment by Advanced Oxidation Process and Their Worldwide Research Trends. *Int. J. Environ. Res. Public Health* **2020**, *17* (1), 170.

(11) Zhiyong, Y.; Ruiying, Q.; Runbo, Y.; Zhiyin, W.; Huanrong, L. Photodegradation Comparison for Methyl Orange by TiO_2, H_2O_2 and KIO_4. *Environ. Technol.* **2018**, *41*, 547−555, DOI: 10.1080/09593330.2018.1505962.

(12) Aziztyana, A. P.; Wardhani, S.; Prananto, Y. P.; Purwonugroho, D.; Darjito. Optimisation of Methyl Orange Photodegradation Using TiO_2-Zeolite Photocatalyst and H_2O_2 in Acid Condition. *IOP Conf. Ser. Mater. Sci. Eng.* **2019**, *546* (4), No. 042047.

(13) Chen, C.; Liu, J.; Liu, P.; Yu, B. Investigation of Photocatalytic Degradation of Methyl Orange by Using Nano-Sized ZnO Catalysts. *Adv. Chem. Eng. Sci.* **2011**, *01* (01), 9−14.

(14) Prabha, D.; Usharani, K.; Ilangovan, S.; Suganya, M.; Balamurugan, S.; Srivind, J.; Nagarethinam, V. S.; Balu, A. R. Visible Light Irradiated Photocatalytic Activity of SnS_2-CdS Nanocomposite against the Degradation of Methyl Orange Dye. *Mater. Technol.* **2018**, *33* (5), 333−339.

(15) Liu, T.; Wang, L.; Lu, X.; Fan, J.; Cai, X.; Gao, B.; Miao, R.; Wang, J.; Lv, Y. Comparative Study of the Photocatalytic Performance for the Degradation of Different Dyes by $ZnIn_2S_4$: Adsorption, Active Species, and Pathways. *RSC Adv.* **2017**, *7* (20), 12292−12300.

(16) Guan, K.; Li, J.; Lei, W.; Wang, H.; Tong, Z.; Jia, Q.; Zhang, H.; Zhang, S. Synthesis of Sulfur Doped g-C_3N_4 with Enhanced Photocatalytic Activity in Molten Salt. *J. Mater.* **2021**, *7* (5), 1131−1142.

(17) Hui, J.; Pestana, C. J.; Caux, M.; Gunaratne, H. Q. N.; Edwards, C.; Robertson, P. K. J.; Lawton, L. A.; Irvine, J. T. S. Graphitic-C_3N_4 Coated Floating Glass Beads for Photocatalytic Destruction of Synthetic and Natural Organic Compounds in Water under UV Light. *J. Photochem. Photobiol. A Chem.* **2021**, *405*, No. 112935.

(18) Lokhande, A. C.; Babar, P. T.; Karade, V. C.; Gang, M. G.; Lokhande, V. C.; Lokhande, C. D.; Kim, J. H. The Versatility of Copper Tin Sulfide. *J. Mater. Chem. A* **2019**, *7* (29), 17118−17182.

(19) Tran, D. A.; Nguyen Pham, C. T.; Nguyen Ngoc, T.; Nguyen Phi, H.; Hoai Ta, Q. T.; Truong, D. H.; Nguyen, V. T.; Luc, H. H.; Nguyen, L. T.; Dao, N. N.; Kim, S. J.; Vo, V. One-Step Synthesis of Oxygen Doped g-C_3N_4 for Enhanced Visible-Light Photodegradation of Rhodamine B. *J. Phys. Chem. Solids* **2021**, *151*, No. 109900.

(20) Wang, F.; Zeng, Q.; Tang, J.; Peng, L.; Shao, J.; Luo, S. Synthesis of g-C_3N_4/CuS Heterojunction with Enhanced Photocatalytic Activity Under Visible-Light. *J. Nanosci. Nanotechnol.* **2020**, *20* (9), 5896−5905.

(21) Gebreslassie, G.; Bharali, P.; Chandra, U.; Sergawie, A.; Baruah, P. K.; Das, M. R.; Alemayehu, E. Hydrothermal Synthesis of g-C_3N_4/$NiFe_2O_4$ Nanocomposite and Its Enhanced Photocatalytic Activity. *Appl. Organomet. Chem.* **2019**, *33* (8), No. e5002.

(22) Abdelhafeez, I. A.; Chen, J.; Zhou, X. Scalable One-Step Template-Free Synthesis of Ultralight Edge-Functionalized g-C_3N_4 Nanosheets with Enhanced Visible Light Photocatalytic Performance. *Sep. Purif. Technol.* **2020**, *250*, No. 117085.

(23) Khurram, R.; Nisa, Z. U.; Javed, A.; Wang, Z.; Hussien, M. A. Synthesis and Characterization of an α-Fe_2O_3-Decorated g-C_3N_4 Heterostructure for the Photocatalytic Removal of MO. *Molecules* **2022**, *27* (4), 1442.

(24) Salehi, G.; Abazari, R.; Mahjoub, A. R. Visible-Light-Induced Graphitic−C_3N_4@Nickel−Aluminum Layered Double Hydroxide Nanocomposites with Enhanced Photocatalytic Activity for Removal of Dyes in Water. *Inorg. Chem.* **2018**, *57* (14), 8681−8691.

(25) Swain, G.; Sultana, S.; Moma, J.; Parida, K. Fabrication of Hierarchical Two-Dimensional MoS_2 Nanoflowers Decorated upon Cubic $CaIn_2S_4$ Microflowers: Facile Approach To Construct Novel Metal-Free p−n Heterojunction Semiconductors with Superior Charge Separation Efficiency. *Inorg. Chem.* **2018**, *57* (16), 10059−10071.

(26) Huy, B. T.; Nhi, P. T.; Vy, N. T. T.; Khanh, D. N. N.; Tho, N. T. M.; Thang, N. Q.; Sy, D. T.; Minh, B. Q.; Phuong, N. T. K. Design of Novel p−n Heterojunction $ZnBi_2O_4$-ZnS Photocatalysts with Impressive Photocatalytic and Antibacterial Activities under Visible Light. *Environ. Sci. Pollut. Res.* **2022**, *29* (56), 84471−84486.

(27) Xin, Z.; Zheng, H.; Hu, J. Construction of Hollow Co_3O_4@$ZnIn_2S_4$ p-n Heterojunctions for Highly Efficient Photocatalytic Hydrogen Production. *Nanomaterials* **2023**, *13* (4), 758.

(28) Minnam Reddy, V. R.; Pallavolu, M. R.; Guddeti, P. R.; Gedi, S.; Yarragudi Bathal Reddy, K. K.; Pejjai, B.; Kim, W. K.; Kotte, T. R. R.; Park, C. Review on Cu_2SnS_3, Cu3SnS4, and Cu_4SnS_4 Thin Films and Their Photovoltaic Performance. *J. Ind. Eng. Chem.* **2019**, *76*, 39−74.

(29) Zhao, B.; Li, S.; Che, M.; Zhu, L. Synthesis of Cu_3SnS_4 Nanoparticles with a Novel Structure as Low-Cost Counter Electrode in Dye-Sensitized Solar Cell. *Int. J. Electrochem. Sci.* **2016**, *11*, 6514−6522.

(30) Maheskumar, V.; Selvaraju, T.; Vidhya, B. Influence of Solvent in Solvothermal Synthesis of Cu_3SnS_4: Morphology and Band Gap Dependant Electrocatalytic Hydrogen Evolution Reaction and Photocatalytic Dye Degradation. *Int. J. Hydrogen Energy* **2018**, *43* (51), 22861−22873.

(31) Wang, J.; Bo, T.; Shao, B.; Zhang, Y.; Jia, L.; Tan, X.; Zhou, W.; Yu, T. Effect of S Vacancy in Cu_3SnS_4 on High Selectivity and Activity of Photocatalytic CO_2 Reduction. *Appl. Catal. B Environ.* **2021**, *297*, No. 120498.

(32) Maheskumar, V.; Vidhya, B. Investigation on the Morphology and Photocatalytic Activity of Cu_3SnS_4 Synthesized by Ball Milling

https://doi.org/10.1021/acsomega.4c02414
ACS Omega 2024, 9, 28463−28475

and Solvothermal Method. *J. Photochem. Photobiol. A Chem.* **2018**, *356*, 521−529.
(33) Olatunde, O. C.; Onwudiwe, D. C. Selective Syntheses of Kuramite (Cu_2SnS_3) and Petrukite (Cu_3SnS_4) Phases of Copper Tin Sulphide, and Their Electrochemical and Photocatalytic Properties. *Results Mater.* **2022**, *13*, No. 100249.
(34) Liu, H.; Chen, Z.; Jin, Z.; Su, Y.; Wang, Y. A Reduced Graphene Oxide Supported Cu_3SnS_4 Composite as an Efficient Visible-Light Photocatalyst. *Dalt. Trans.* **2014**, *43* (20), 7491.
(35) Jiang, X.; Zhu, Y.; Liu, X.; Sun, W.; Guo, S.; Men, Y. Synthesis of Flower-like Cu_3SnS_4 Microspheres and Cu_3SnS_4/Reduced Graphene Oxide Composite with High Photocatalytic Activity. *Colloid Interface Sci. Commun.* **2021**, *41*, No. 100360.
(36) Sebastian, A.; Maheskumar, V.; Bhuvanesh, N.; Vidhya, B.; Nandhakumar, R.; Jiang, Z. Photocatalytic Performance of Cu_3SnS_4 (CTS)/Reduced Graphene Oxide (RGO) Composite Prepared via Ball Milling and Solvothermal Approach. *J. Mater. Sci. Mater. Electron.* **2020**, *31* (23), 21408−21418.
(37) Sharma, N.; Das, T.; Kumar, S.; Bhosale, R.; Kabir, M.; Ogale, S. Photocatalytic Activation and Reduction of CO_2 to CH_4 over Single Phase Nano Cu_3SnS_4: A Combined Experimental and Theoretical Study. *ACS Appl. Energy Mater.* **2019**, *2* (8), 5677−5685.
(38) Tian, Y.; Zhang, J.; Yang, X.; Jia, D. Facile One-Pot Synthesis and Enhanced Photocatalytic Performances of Ternary Metal Sulfide Composite g-C_3N_4/Cu_3SnS_4. *Eur. J. Inorg. Chem.* **2022**, *2022* (19), No. e202200151.
(39) Li, Y.; Liu, F.; Chang, Y.; Wang, J.; Wang, C. High Efficient Photocatalytic Activity from Nanostructuralized Photonic Crystal-like p-n Coaxial Hetero-Junction Film Photocatalyst of Cu_3SnS_4/TiO_2 Nanotube Arrays. *Appl. Surf. Sci.* **2017**, *426*, 770−780.
(40) Han, Y.; Yang, Y.; Zhao, J.; Yin, X.; Que, W. Facile One-Pot Synthesis of Ternary Copper-Tin-Chalcogenide Quantum Dots on Reduced Graphene Oxide for Enhanced Photocatalytic Activity. *Catal. Lett.* **2018**, *148* (10), 3112−3118.
(41) Zaman, M. B.; Poolla, R. Morphological Tuning of Hydrothermally Derived Visible Light Active Cu_2SnS_3 Nanostructures and Their Applications in Photocatalytic Degradation of Reactive Industrial Dyes. *Opt. Mater. (Amst).* **2020**, *104*, No. 109853.
(42) Olatunde, O. C.; Onwudiwe, D. C. A Comparative Study of the Effect of Graphene Oxide, Graphitic Carbon Nitride, and Their Composite on the Photocatalytic Activity of Cu_3SnS_4. *Catalysts* **2022**, *12* (1), 14.
(43) Fang, H.; Luo, Y.; Zheng, Y.; Ma, W.; Tao, X. Facile Large-Scale Synthesis of Urea-Derived Porous Graphitic Carbon Nitride with Extraordinary Visible-Light Spectrum Photodegradation. *Ind. Eng. Chem. Res.* **2016**, *55* (16), 4506−4514.
(44) Chidhambaram, N.; Ravichandran, K. Single Step Transformation of Urea into Metal-Free g-C_3N_4 Nanoflakes for Visible Light Photocatalytic Applications. *Mater. Lett.* **2017**, *207*, 44−48.
(45) Li, J.; Luo, F.; Zhao, Q.; Liu, W.; Xiao, D. Low-Temperature Coprecipitation Synthesis of Amorphous Nickel Cobalt Sulfide Nanoparticles for High-Performance Supercapacitors. *J. Mater. Sci. Mater. Electron.* **2019**, *30* (15), 14538−14546.
(46) Wang, S.; Li, W.; Xin, L.; Wu, M.; Lou, X. High-Performance Nickel Cobalt Sulfide Materials via Low-Cost Preparation for Advanced Asymmetric Supercapacitors. *RSC Adv.* **2016**, *6* (48), 42633−42642.
(47) Liu, J.; Zhang, T.; Wang, Z.; Dawson, G.; Chen, W. Simple Pyrolysis of Urea into Graphitic Carbon Nitride with Recyclable Adsorption and Photocatalytic Activity. *J. Mater. Chem.* **2011**, *21* (38), 14398.
(48) Paul, D. R.; Sharma, R.; Nehra, S. P.; Sharma, A. Effect of Calcination Temperature, PH and Catalyst Loading on Photodegradation Efficiency of Urea Derived Graphitic Carbon Nitride towards Methylene Blue Dye Solution. *RSC Adv.* **2019**, *9* (27), 15381−15391.
(49) Hussain, S. K.; Yu, J. S. Surfactant-Free One-Pot Hydrothermal Growth of Micro-Flower-Like Copper Tin Sulfide Electrode Material for Pseudocapacitor Applications. *J. Electrochem. Soc.* **2018**, *165* (11), E592−E597.
(50) Hadi, Z. L.; Essa, M. S.; Chiad, B. T. Ternary Cu_2SnS_3 Thin Films Deposited by Fully Controlled System of Spray Pyrolysis. *J. Phys. Conf. Ser.* **2019**, *1234*, No. 012041.
(51) Kadam, S. L.; Bulakhe, R. N.; Kadam, R. A.; Yewale, M. A. Electrochemical Synthesis of CuS Thin Film for Supercapacitor Application. *Macromol. Symp.* **2020**, *392* (1), No. 1900209.
(52) Zhang, Z.; Huang, J.; Zhang, M.; Yuan, Q.; Dong, B. Ultrathin Hexagonal SnS_2 Nanosheets Coupled with g-C_3N_4 Nanosheets as 2D/2D Heterojunction Photocatalysts toward High Photocatalytic Activity. *Appl. Catal. B Environ.* **2015**, *163*, 298−305.
(53) Tipcompor, N.; Thongtem, S.; Thongtem, T. Characterization of Cu_3SnS_4 Nanoparticles and Nanostructured Flowers Synthesized by a Microwave-Refluxing Method. *Jpn. J. Appl. Phys.* **2013**, *52* (11R), No. 111201.
(54) Hu, H.; Liu, Z.; Yang, B.; Chen, X.; Qian, Y. Template-Mediated Growth of Cu_3SnS_4 Nanoshell Tubes. *J. Cryst. Growth* **2005**, *284* (1−2), 226−234.
(55) Tipcompor, N.; Thongtem, S.; Thongtem, T. Effect of Microwave Radiation on the Morphology of Tetragonal Cu_3SnS_4 Synthesized by Refluxing Method. *Superlattices Microstruct.* **2015**, *85*, 488−496.
(56) Xiong, Y.; Xie, Y.; Du, G.; Su, H. From 2D Framework to Quasi-1D Nanomaterial: Preparation, Characterization, and Formation Mechanism of Cu_3SnS_4 Nanorods. *Inorg. Chem.* **2002**, *41* (11), 2953−2959.
(57) Jathar, S. B.; Rondiya, S. R.; Jadhav, Y. A.; Nilegave, D. S.; Cross, R. W.; Barma, S. V.; Nasane, M. P.; Gaware, S. A.; Bade, B. R.; Jadkar, S. R.; Funde, A. M.; Dzade, N. Y. Ternary Cu_2SnS_3: Synthesis, Structure, Photoelectrochemical Activity, and Heterojunction Band Offset and Alignment. *Chem. Mater.* **2021**, *33* (6), 1983−1993.
(58) Pourshirband, N.; Nezamzadeh-Ejhieh, A. An Efficient Z-Scheme CdS/g-C_3N_4 Nano Catalyst in Methyl Orange Photodegradation: Focus on the Scavenging Agent and Mechanism. *J. Mol. Liq.* **2021**, *335*, No. 116543.
(59) Li, Y.; Huo, H.; Wang, X.; Xia, Y.; Zhang, A.; Gao, L. Enhancement of Photocatalysis Performance of $CdIn_2S_4$/g-C_3N_4 Heterojunction by H_2O_2 Synergism. *J. Mater. Sci. Mater. Electron.* **2021**, *32* (11), 14218−14234.
(60) Ran, Q.; Yu, Z.; Jiang, R.; Hou, Y.; Huang, J.; Zhu, H.; Yang, F.; Li, M.; Li, F.; Sun, Q. A Novel, Noble-Metal-Free Core-Shell Structure Ni-P@C Cocatalyst Modified Sulfur Vacancy-Rich $ZnIn_2S_4$ 2D Ultrathin Sheets for Visible Light-Driven Photocatalytic Hydrogen Evolution. *J. Alloys Compd.* **2021**, *855*, No. 157333.
(61) Nagaleekar, T. M.; Sharma, N.; Das, T.; Varhade, S.; Badadhe, S. S.; Thotiyl, M. O.; Kabir, M.; Ogale, S. A Combined Experimental and Computational Study of Gas Sensing by Cu_3SnS_4 Nanoparticulate Film: High Selectivity, Stability, and Reversibility for Room Temperature H_2S Sensing. *Adv. Mater. Interfaces* **2018**, *5* (10), No. 1701492.
(62) Shenoy, S.; Tarafder, K. Enhanced Photocatalytic Efficiency of Layered CdS/CdSe Heterostructures: Insights from First Principles Electronic Structure Calculations. *J. Phys.: Condens. Matter* **2020**, *32* (27), 275501.
(63) Zhang, X.; Tang, Y.; Wang, Y.; Shen, L.; Gupta, A.; Bao, N. Simple One-Pot Synthesis of Cu_4SnS_4 Nanoplates and Temperature-Induced Phase Transformation Mechanism. *CrystEngComm* **2020**, *22* (7), 1220−1229.
(64) Zhang, X. Y.; Liu, S. G.; Zhang, W. J.; Wang, X. H.; Han, L.; Ling, Y.; Li, N. B.; Luo, H. Q. Photoelectrochemical Platform for Glucose Sensing Based on g-C_3N_4/$ZnIn_2S_4$ Composites Coupled with Bi-Enzyme Cascade Catalytic in-Situ Precipitation. *Sensors Actuators B Chem.* **2019**, *297*, No. 126818.
(65) Li, Y.; Ling, W.; Han, Q.; Kim, T. W.; Shi, W. Localized Surface Plasmon Resonances and Its Related Defects in Orthorhombic Cu_3SnS_4 Nanocrystals. *J. Alloys Compd.* **2015**, *633*, 347−352.
(66) Naikwade, A. G.; Jagadale, M. B.; Kale, D. P.; Gophane, A. D.; Garadkar, K. M.; Rashinkar, G. S. Photocatalytic Degradation of

https://doi.org/10.1021/acsomega.4c02414
ACS Omega 2024, 9, 28463−28475

Methyl Orange by Magnetically Retrievable Supported Ionic Liquid Phase Photocatalyst. *ACS Omega* **2020**, *5*, 131−144.
(67) Kuldeep, A. R.; Dhabbe, R. S.; Garadkar, K. M. Development of g-C_3N_4-TiO_2 Visible Active Hybrid Photocatalyst for the Photodegradation of Methyl Orange. *Res. Chem. Intermed.* **2021**, *47* (14), 5155−5174.
(68) Lu, M.; Pei, Z.; Weng, S.; Feng, W.; Fang, Z.; Zheng, Z.; Huang, M.; Liu, P. Constructing Atomic Layer g-C_3N_4−CdS Nanoheterojunctions with Efficiently Enhanced Visible Light Photocatalytic Activity. *Phys. Chem. Chem. Phys.* **2014**, *16* (39), 21280−21288.

https://doi.org/10.1021/acsomega.4c02414
ACS Omega 2024, 9, 28463−28475